

行政院國家科學委員會補助專題研究計畫 成果報告
 期中進度報告

銻化物基材之量子結構及元件

計畫類別： 個別型計畫 整合型計畫

計畫編號：

執行期間：96年8月1日至99年7月31日

執行機構及系所：國立交通大學電子工程學系

計畫主持人：李建平

共同主持人：

計畫參與人員：

成果報告類型(依經費核定清單規定繳交)： 精簡報告 完整報告

本計畫除繳交成果報告外，另須繳交以下出國心得報告：

- 赴國外出差或研習心得報告
- 赴大陸地區出差或研習心得報告
- 出席國際學術會議心得報告
- 國際合作研究計畫國外研究報告

處理方式：除列管計畫及下列情形者外，得立即公開查詢

- 涉及專利或其他智慧財產權， 一年 二年後可公開查詢

Content

Abstract (Chinese)	3
Abstract (English)	4
1. Introduction	5
2. Research method	6
2-1 mid-infrared light source	6
2-2 magneto-optical properties of type-II GaAs QDs in GaSb matrix	8
2-3 Sb-based high speed electronic devices	9
3. Results and discussions	10
3-1 mid-infrared light source	10
3-2 magneto-optical properties of type-II GaAs QDs in GaSb matrix	14
3-3 Sb-based high speed electronic devices	21
4. Conclusion	24
Reference	25

摘要

國立交通大學 電子工程系

計畫名稱：銻化物基材之量子結構及元件

研究者：李建平

經費來源：行政院國家科學委員會

關鍵詞：銻化合物；W 量子井；中紅外線；type II 量子點；異質結構場效電晶體

在此研究計畫，首先，我們利用分子束磊晶方式在磷化銦基板上成長一砷化銦銻/銻砷化銻/砷化銦鋁銻/砷化銦鋁—第二型”W”量子井結構來研究中紅外光源。我們第一次在此材料系統上成功展示出室溫光激發螢光波長可超過 2.56 微米。我們所設計製備的樣品其發光峰值在低溫下可橫跨 2 到 2.5 微米的廣闊範圍。樣品品質十分良好，從低溫(35K)到室溫其積分的光激發螢光強度只大約衰減十倍。我們發現光激發螢光強度會隨著增加發光波長而衰減，這是由於電子電洞波函數重疊變少所致。這與理論計算一致。在變化激發光強度的螢光實驗裡，”W”量子井的發光峰值會隨著增加激發光強度而藍移，然而其關係卻不遵隨第二型異質介面 1/3 次方的規則，局部態填滿效應能對此現象提供一個合理的解釋。

其次，我們觀察了第二型張應力砷化銻自組式量子點的磁光響應。藉由沉積不同厚度的砷化銻，我們可以調整量子點的尺寸與對應的發光能量。利用逆磁偏移的實驗結果，我們分析不同量子點的載子波函數，我們發現，隨著發光能量的增加，也就是量子點尺寸的減縮，逆磁係數首先會快速提升之後會在 $21 \mu\text{eV}/\text{T}^2$ 飽和。根據一個簡化的計算模型，這個不尋常的趨勢是被歸因於，當量子點變小時，電子逐漸移出量子點到沾濕層，這個去侷限化效應在這個材料系統會被強化，因為量子點的應力鬆弛釋放會提昇導帶最底能量使之超過沾濕層。

最後，我們研究銻化物異質結構場效電晶體。我們提出一個新的複合式通道的設計來實現具有高電子遷移率及高崩潰電壓的銻化物高速電子元件，此複合式通道由銻砷化銦及砷化銦構成。此外，我們還設計了新穎的緩衝層結構來改善元件的漏電問題。我們成功的以分子束磊晶成長出具電子遷移率 $\sim 12000 \text{ cm}^2/\text{Vs}$ 的樣品，所製作的元件顯示良好的調變特性及在通道關閉的情形下有較低的緩衝層漏電。

Abstract

Department of Electronics Engineering, National Chiao-Tung University

Title : Physics and Device Antimonide-based Quantum Structure and Devices

Principal Investigator : Chien-Ping Lee

Sponsor : National Science Council

Keywords : Antimonide,, “W” quantum wells, mid-infrared, type II quantum dot, heterostructure FET,

In this project, first, we investigated the mid-infrared light source based on the InGaAs/GaAsSb/InAlGaAs/InAlAs type-II “W” quantum wells (QWs) grown on InP substrates by molecular beam epitaxy. The photoluminescence (PL) emission wavelength longer than 2.56 μm at room temperature (RT) is demonstrated for the first time in this material system. The PL emission peaks of our designed samples can cover a wide range from 2 to 2.5 μm at cryogenic temperature. The samples show good optical quality that the reduction of integrated PL intensity is only around one order of magnitude from 35K to RT. We found that the integrated PL intensity decreased as the emission wavelength increased, which is due to the reduction of the electron-hole wavefunction overlap. This is consistent with the calculated result. In the power dependent PL measurements, the emission peak of “W” type QWs show blue shifts with the excitation power (P_{ex}) but does not follow the $P_{\text{ex}}^{1/3}$ rule as predicted by type-II band bending model. The localized states filling effect gives reasonable explanations for the observed phenomena.

Next, the magneto-optical response of type-II tensily-strained GaAs self-assembled quantum dots in GaSb was investigated in magnetic fields up to 14 T. By depositing different GaAs amount, the dot sizes and the corresponding emission energies varied. We analyzed the carrier wave function extent of different dots using the diamagnetic shift results. It was found that, with the increase of the energy (the reduction of the dot size), the diamagnetic coefficient first rises quickly and then saturates at around 21 $\mu\text{eV}/\text{T}^2$. Based on a simple calculation model, this unusual tendency is attributed to the electrons gradually spilling out of the quantum dot to the wetting layer as the dots get smaller. This delocalization effect is enhanced in this material system due to the tensile strain relaxation within the dots, which raises the conduction band edge over that in the wetting layer.

Finally, we studied Sb-based heterostructure FETs (HFETs). In this work, we proposed a composite channel which consisted of an InAsSb channel and an InAs subchannel to realize high channel mobility and high breakdown voltage. In addition, we designed a new buffer layer structure which incorporated AlSb and InSb QDs to improve the device buffer leakage problem. We successfully grew samples with electron mobility 12000 cm^2/Vs . The devices showed good modulation characteristics and lower buffer leakage current (1.5 mA) at pinch-off condition.

1. Introduction

Antimonite compound semiconductors have many unique properties different from conventional semiconductor materials. For example, InSb, the III-V material with the largest lattice constant, has the highest electron mobility of all semiconductors. GaSb, which has similar bandgap as Ge, has one of the highest hole mobility of all semiconductors. The combinations of III-Sb materials offer the possibilities of making light emitters and detectors operating in the wavelengths of mid-infrared, the wavelength range that is important for air pollution monitoring [1,2]. With the ever growing concern on the carbon emission and environmental protection, the monitoring and the control of the air quality have become one of the highest priorities of all countries. So the development of Sb-based devices for mid-infrared applications has generated a lot of interests recently.

The mid-IR lasers with wavelengths in the 2-3 μm range have been fabricated on GaSb substrates using InGaAsSb/AlGaAsSb type-I quantum wells (QWs) [3,4]. It is, however, much more desirable to use a more popular substrate such as InP, which is cheaper, has a better quality and has a better thermal conductivity. But to grow type-I QWs with emission wavelength longer than 2 μm on InP is difficult due to lattice mismatch [5]. The longest wavelength reported is 2.33 μm with a highly strained InAs/InGaAs system [6]. However, if we use the type-II InGaAs/GaAsSb heterostructure on InP substrates, we can bypass the requirement for small band gap materials by using the staggered band alignment and the wavelength can be extended longer without being limited by the band gap of the constituent materials.

In addition to the applications of the mid-infrared, the unique Type-II junctions and nanostructures formed by antimonide and other III-V semiconductors exhibit many new physical properties and the possible applications. For example, type-II self-assembled quantum dots (SAQDs) have attracted considerable interest for the application of carrier storage [7], spin storage device [8], and the exhibition of optical Aharnov-Bohm effect in magnetic fields [9, 10] owing to the spatial separation between the electrons and holes. To date, most SAQD structures are fabricated by the natural compressive strain due to the lattice mismatch between different materials. Recently, the QD formation driven by tensile strain in the GaAs/GaSb type-II heterostructure with GaAs dots in GaSb matrix has been reported. The mid-IR optical response of the type-II transition is able to be extended to a longer wavelength because of the band gap shrinkage induced by tensile strain [11].

Besides, the Sb-based binary compound semiconductor AlSb, GaSb, InSb and InAs together with their related alloys are candidates for high-speed, low power electronic devices [12]. Due to the narrow band gap of InAs (0.36 eV) and InSb (0.18 eV) channel materials, impact ionization effects can become dominant for short gate lengths as drain bias exceeds the energy gap in the channel. Further, because the staggered band lineup at the InAs/AlSb heterojunctions leaves holes without confinement, some of the impact-ionized holes are drawn into negatively bias gate, giving rise to a significant gate leakage component, others accumulate in the buffer layers and induce nonsaturating drain characteristics by the feedback mechanism, known as the kink effects. Proposed approaches to improve breakdown including the use of a back gate [13], increased quantum confinement [14], dual gating [15], additional InAs subchannel [16], composite channel like InAs/InAsP and InAs/InAlAs [17,18] and InAsSb channel [19]. However, the improvement in breakdown voltage is still limited thus far, which will largely limit the allowable device operation range.

In this work, first, the mid-IR light sources between 2 μm to 3 μm were studied using the type-II “W” type QWs. We demonstrated that the emission wavelength can be extended longer than 2.56 μm at room

temperature. Next, we studied the magneto-optical properties of GaAs QDs in GaSb matrix. Because of the type-II band alignment, electrons are localized in GaAs QDs while holes are confined to the GaSb region next to GaAs by the Coulomb interaction. As the size of the QDs is changed, an unusual correlation was found between the diamagnetic coefficient and the emission energy. We attributed this phenomenon to the weak localization of electrons within the small-sized QDs in the tensily-strained system. A theoretical model was proposed and the calculated results agree very well with the experimental findings.

In addition to the above works, we also studied an Sb-based heterostructure FET (HFET) with high mobility and high breakdown voltage. In this work, we proposed a composite channel which consisted of an InAsSb channel and an InAs subchannel to realize high channel mobility and high breakdown voltage. In addition, we designed a new buffer layer structure which incorporated AlSb and InSb QDs to improve the device buffer leakage problem. We successfully grew samples with electron mobility $12000 \text{ cm}^2/\text{Vs}$. The devices showed good modulation characteristics and lower buffer leakage current (1.5 mA) at pinch-off condition.

2. Research method

2-1 Mid-IR light source

The structure of a “W” type QW used in this work is composed of symmetric InGaAs/GaAsSb/InGaAs layers, which are sandwiched between two InAlAs barrier layers, lattice matched to InP. The barrier layers provide a strong quantum confinement to enhance the electron-hole wave function overlap and hence the optical matrix element. The band alignment of a represented $\text{In}_{0.53}\text{Ga}_{0.47}\text{As}$ (lattice-matched to InP)/ $\text{GaAs}_{0.4}\text{Sb}_{0.6}$ ($\sim 0.7\%$ compressive strain)/ $\text{In}_{0.52}\text{Al}_{0.48}\text{As}$ “W” structure is shown in Fig. 1(a). In order to optimize the structure, we first calculated the emission wavelength and the amount of electron-hole wavelength overlap by solving the Schrodinger equation using the effective mass approximation with the parameters taken from the previous articles [21-23]. Fig. 1(b) and Fig. 1(c) respectively show the layer thickness dependence of the “W” type QWs emission wavelength and the electron-hole wavefunction overlap. Basically, wavelength can be tuned in the range from 1.8 to 3 μm via modifying the thickness of InGaAs and GaAsSb. However, the wavefunction overlap decreases when the emission wavelength is increased, as indicating in Fig. 1(c). This is an intrinsic feature for the “W” type QW. The electron and hole are confined separately in different layers, the electron in the two coupled InGaAs layers and the hole in the GaAsSb layer, as shown in Fig. 1(a). Since the confinement potentials are large ($>0.4\text{eV}$) for both carriers, the quantization energies are decided by their own layer thickness; a thicker InGaAs or GaAsSb layer leads to a smaller electron or hole quantization energy and hence a longer emission wavelength. Although the increase of the InGaAs or GaAsSb layer thickness extends the emission wavelength, it also makes the electron and hole wave functions more concentrated in individual layers, and causes the reduction of electron-hole overlap. Obviously, it is a trade-off between the long wavelength emission and the optical matrix element [20]. Although the wavelength can be extended with more Sb content in GaAsSb, the raised conduction band edge, however, blocks the electron wave function penetration into the GaAsSb layer causing a reduction of the electron-hole wave function overlap. So it is still a trade-off situation. Since the optical matrix element is an important parameter for optoelectronic devices, structure optimization of the “W” type QWs is very important.

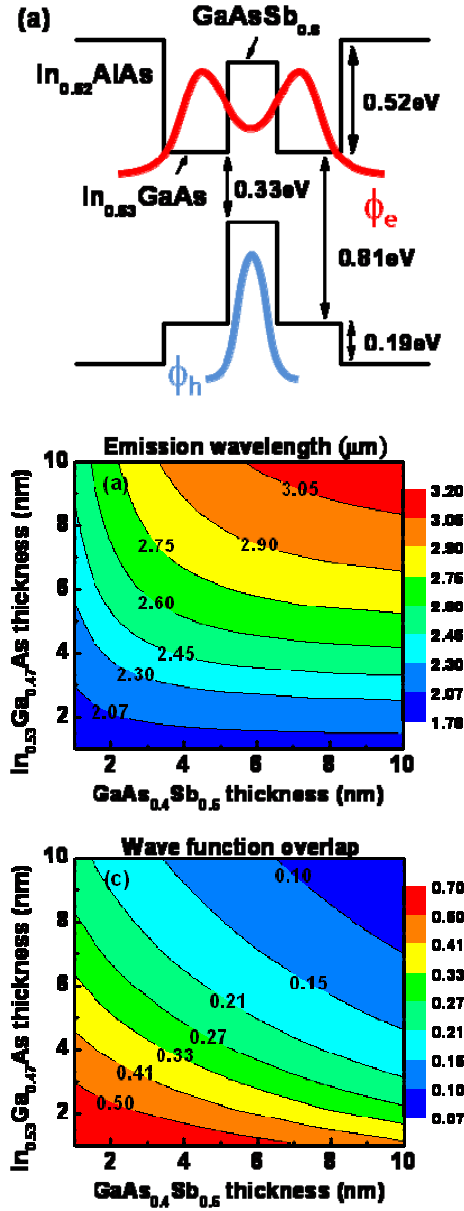


Fig. 1(a) Energy band diagram of the “W” type QW with the wavefunctions for electron and hole. Calculated contour plots of (b) emission wavelength and (c) electron-hole wavefunction overlap versus InGaAs (vertical axis) and GaAsSb (horizontal axis) layer thickness.

Our samples were grown on S-doped (001) InP substrates by a Veeco GEN II solid-source molecular beam epitaxy system. The As_2 and Sb_2 species were used through the equipped needle-valve controlled cracking cells. The wafer surface temperature was monitored by an infrared pyrometer. For the multilayer growth consideration, the structure of the “W” QWs designed here are the symmetric $\text{In}_{0.53}\text{Ga}_{0.47}\text{As}/\text{GaAsSb}/\text{In}_{0.53}\text{Ga}_{0.47}\text{As}$ layers sandwiched between two 2 nm $\text{In}_{0.36}\text{Al}_{0.32}\text{Ga}_{0.32}\text{As}$ tensile strain layers to compensate the compressive strain in the GaAsSb layer. Nine such “W” type QWs spaced by 25 nm $\text{In}_{0.52}\text{Al}_{0.48}\text{As}$ barrier layers were grown and placed between two 200 nm $\text{In}_{0.52}\text{Al}_{0.48}\text{As}$ layers, as shown in Fig 2. In order to optimize the “W” structure, this study was performed systematically by varying the thickness of

the InGaAs/GaAsSb layers, the composition of the GaAsSb layer and the growth temperature. The growth parameters are listed in Table 1, where three series of samples are grouped and labeled as A, B, and C. Groups A and B are samples with variable thicknesses of InGaAs and GaAsSb, respectively. Group C contains samples with different Sb mole fraction in the GaAsSb layer by adjusting the Sb_2/As_2 beam equivalent pressure (BEP) ratio. The growth temperature is also changed from group A to group C.

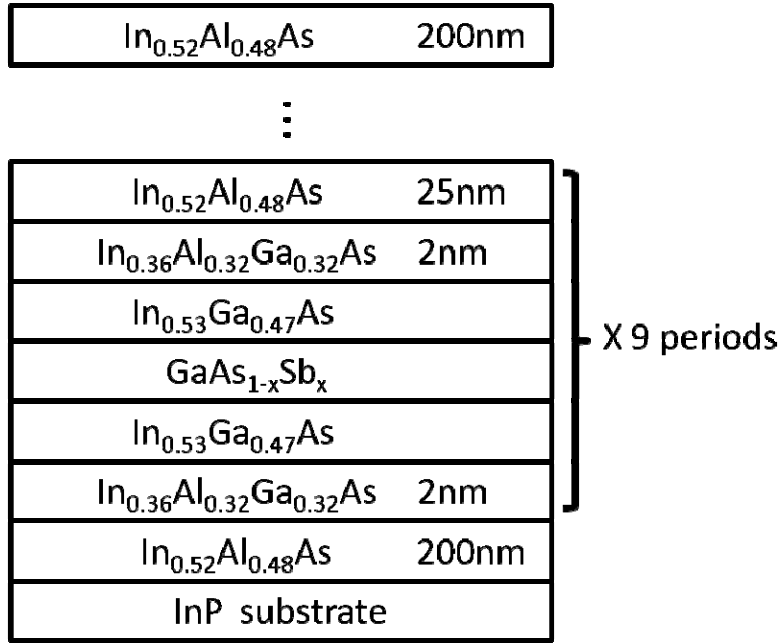


Fig. 2 The structure of the designed “W” type QWs.

Sample number	Layer thickness(nm)			BEP ratio Sb_2/As_2	Growth T(°C)	λ_{peak} (μm)	FWHM (meV)
	$In_{0.53}GaAs$ (lattice match)	$GaAs_{1-x}Sb_x$	x				
A1	4	3	0.58	1.8	475	2.05	24.7
A2	7	3	0.58	1.8	475	2.34	22.4
A3	10	3	0.58	1.8	475	2.47	25.4
B1	5	2	0.65	2.0	470	2.17	22.7
B2	5	3	0.65	2.0	470	2.27	18.8
B3	5	4	0.65	2.0	470	2.42	13.9
C1	4	3	0.74	1.8	460	2.37	12.6
C2	4	3	0.78	2.9	460	2.48	13.8

Table 1 The InGaAs/GaAsSb layer thickness, the Sb_2/As_2 BEP ratio, the summarized PL peak wavelength, and FWHM of the “W” type QW samples in group A, B, and C.

2-2 Magneto-optical properties of type-II GaAs QDs in GaSb matrix

The GaAs QDs were grown on n+ GaSb (001) substrates by a Veeco Gen-II molecular beam epitaxy (MBE) system with valve cracker sources of Sb₂ and As₂ molecules. Three samples with different amount of deposited GaAs for QD formation were prepared. They were: (1) sample A with 2.0 monolayers (ML) of GaAs, (2) sample B with 2.3 MLs of GaAs, and (3) sample C with 2.5 ML of GaAs. The growth temperature was 500 °C, the V/III beam equivalent pressure (BEP) ratio for GaAs was 3, and the growth rate was 0.1 ML/s, which was taken from that of 0.086 ML/s for GaAs homoepitaxial growth calibrated using RHEED oscillation. To improve the GaAs QD uniformity, the migration enhanced epitaxy (MEE) technique was used for the QD growth. A 2 seconds growth interruption was used after every 0.5 ML of GaAs was deposited. The GaAs QD layer was embedded in a 100 nm GaSb matrix, which was sandwiched with two 20 nm Al_{0.3}Ga_{0.7}Sb barriers. These barriers were used to confine carriers and thus improve the PL intensity.

The embedded GaAs QDs were characterized by a transmission electron microscope (JEOL 2010F TEM) operated at 200 keV. The TEM specimens were prepared using cross-section and plan-view thinning in a Gatan 691 ion mill. Conventional photoluminescence (PL) and magneto-PL measurement were performed at 1.4 K with a 14 Tesla superconducting magnet. The excitation source was a 532 nm Nd:Yag laser coupled through an optical fiber with a focusing lens. The PL signal was collected with a fiber bundle, dispersed by a 500 mm monochromator, and detected by a wavelength-extended InGaAsSb detector.

The embedded GaAs QDs were characterized by a transmission electron microscope (JEOL 2010F TEM) operated at 200 keV. The TEM specimens were prepared using cross-section and plan-view thinning in a Gatan 691 ion mill. Magneto-photoluminescence (PL) measurement was performed at 1.4 K in high magnetic fields up to 14 Tesla in a Faraday configuration. The excitation source was a 532 nm Nd:Yag laser coupled through an optical fiber with a focusing lens. The PL signal was collected with a fiber bundle, dispersed by a 500 mm monochromator, and detected by a wavelength-extended InGaAsSb detector.

2-3 Sb-based high speed electronic devices

The objective of this work is to design an Sb-based heterostructure FET (HFET) with high mobility and higher breakdown voltage. In order to obtain high mobility, InAs or InSb was used as channel material. In order to further improve breakdown voltage, band gap engineering was employed to effectively enlarge the band gap of channel material. From the diagram of band gap vs. lattice constant, shown in Fig. 3 [12], we can find many materials with a band gap greater than 1 eV. However, most of them have a lattice constant less than 6 Å, which actually can not be used as the candidate material due to the large lattice mismatch with InAs or InSb. The materials with lattice constant ranging from 6 Å to 6.5 Å, including GaSb, AlSb, InAs, InSb and their alloy, are proper candidates. For InAs channel, lattice constant ranging from 6 Å to 6.2 Å is the range of interest. In particular, as the lattice constant is 6.2 Å, some advantages can be obtained as follows [19,24]. First, the barrier material InAlSb with Indium content (In=0.2) and the high-mobility channel material InAsSb with antimony content (Sb=0.35) are lattice-matched. Second, the barrier InAlSb (In=0.2) and channel InAsSb (Sb=0.35) formed type I heterojunction, which can avoid the problems that occurred in type II InAs/AlSb heterojunction. Besides, the strain effect plays a key role in the actual band gap as we grow material with different lattice constant. Depending on the stress type and the amount of lattice match between two different materials, the final magnitude of band gap changed significantly. Fig. 4 showed the theoretical calculation of the band gap with the quantum well lattice constant, for the case of strained quantum well on

the GaSb substrate [25]. As the lattice constant is equal to 6.2\AA , the conduction band offset (ΔE_c) and valance band offset (ΔE_v) between InAs and InAsSb are around 0.1 eV and 0.24 eV, respectively. Therefore, by inserting a thin layer of InAs layer in the middle of the InAsSb (Sb=0.35) channel, taking advantage of the large valance band offset ($\Delta E_v=0.24\text{eV}$) between InAs and the InAsSb channel, the band gap of the InAs/InAsSb composite channel can be effectively enlarged, as shown in Fig.5.

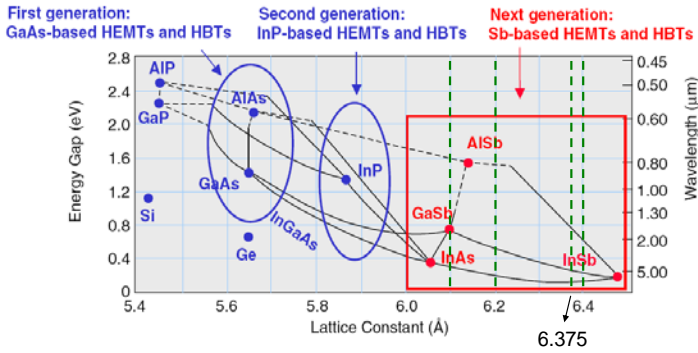


Fig. 3 the diagram of energy gap and lattice constant, with lattice constant ranging from 5.4\AA to 6.5\AA

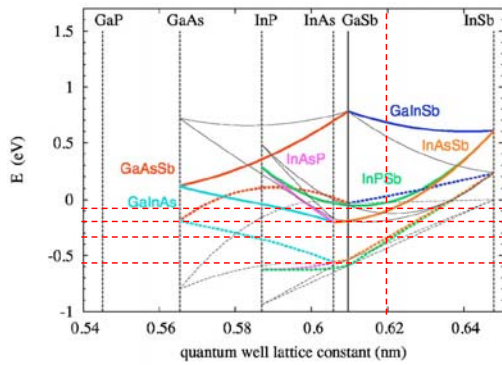


Fig. 4 Band edge diagram of alloyed strained wells on GaSb

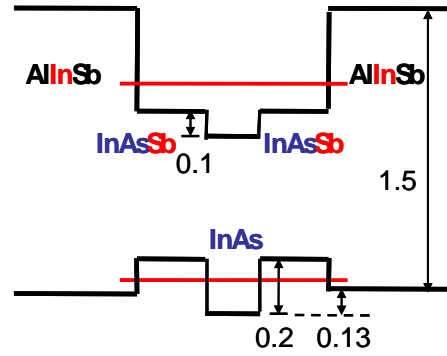


Fig. 5 the schematic band diagram of the designed channel structure

3. Results and discussion

3-1 Mid-IR light sources

After the samples were grown, the photoluminescence (PL) measurement was carried out using a 488nm Ar^+ laser as the excitation source and a thermal electric cooled InGaAs(Sb) detector. All the PL spectra were calibrated by the response spectrum of a 1000°C black radiation source. The PL spectra measured at 20K are presented in Fig 6(a). The peak emission wavelength (λ_{peak}) covers the range from $\sim 2\ \mu\text{m}$ to $\sim 2.5\ \mu\text{m}$. As summarized in Table 1, the λ_{peak} can be extended from $2.05\ \mu\text{m}$ to $2.47\ \mu\text{m}$ by increasing the InGaAs layer thickness from 4 nm to 10 nm as shown in group A, and can be extended from $2.17\ \mu\text{m}$ to $2.42\ \mu\text{m}$ with the increase of GaAsSb layer thickness from 2 nm to 4 nm (in group B). The sensitivity of λ_{peak} to the InGaAs/GaAsSb layer thicknesses agrees well with our calculations. Notice that the full width of half to maximum (FWHM) of the PL spectra increases from 13.9meV to 22.7meV when the GaAsSb layer thickness

is reduced, as indicated in group B. This is caused by the energy level broadening due to the thickness fluctuation when the GaAsSb layer is thin. The λ_{peak} can be also extended by the increase of the Sb-content, as shown by group C samples. The Sb fraction is determined by fitting the λ_{peak} with the calculation results. The λ_{peak} goes from 2.37 μm to 2.48 μm , around a 23 meV difference, as the Sb mole fraction increases from 0.74 to 0.78. We can also see the effect of growth temperature by comparing these three groups of samples. It is found that the samples grown at a lower temperature have a longer emission wavelength and a narrower PL spectrum. This may indicate that the Sb incorporation is more efficient and the fluctuation of alloy composition is less at lower growth temperatures [26,27]. Figure 6(b) shows the integrated PL intensity as a function of the emission wavelength. It clearly shows the trade-off situation as predicted by the simulation. The calculated curve, which is based on the assumption that the integrated PL intensity is proportional to the square of the wave function overlap, fits very nicely with the experimental results.

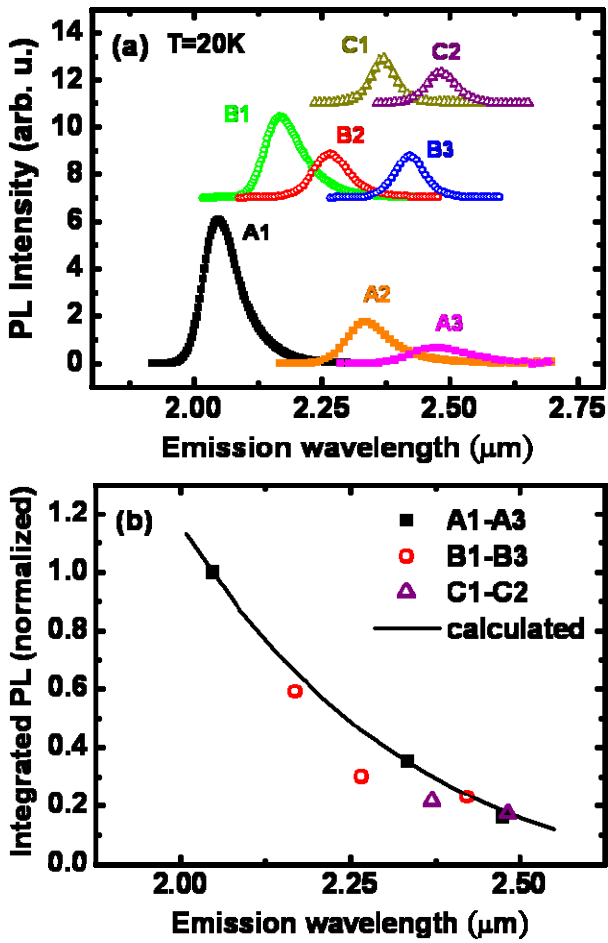


Fig. 6 (a) PL spectra of samples in group A, B, C, and (b) integrated PL intensity (normalized at sample A1) plotted against the peak wavelength. The calculated result is plotted as the solid curve.

The optical transition of the type-II heterostructure has been extensively studied previously [28,29]. The λ_{peak} usually blue shifts with the excitation power (P_{ex}), and the amount of shift is linearly dependent on the one-third power of P_{ex} because of the band bending effect caused by the accumulation of spatially separated electrons and holes in the adjacent triangular interface potential wells. However, the power dependent emission of a “W” type QW has never been studied in detail. We found that, although λ_{peak} shifts to a shorter

wavelength as P_{ex} is increased, the energy shift does not obey the $P_{\text{ex}}^{1/3}$ law, especially under low P_{ex} . The power dependent spectra of sample A1 and C1 are presented in Fig. 7(a), and the amount of energy shift is plotted as a function of the P_{ex} in Fig. 7(b) along with the ideal $P_{\text{ex}}^{1/3}$ curve for comparison (both axes in log scale). Since the curves are not linear in this log-log plot, the energy shift vs. P_{ex} does not follow any power law. We also notice that sample A1 has a more pronounced energy shift than sample C1. This power dependent behavior is not due to the heating effect since the integrated PL intensity is linearly proportional to P_{ex} , as shown in the inset of Fig. 7(b). The possible reason for the amount of blue shift to deviate from the $P_{\text{ex}}^{1/3}$ law is the state filling effect of the localized states. The localized states are caused by interface roughness and alloy composition fluctuation, which are common in the ternary alloy [30,31]. Under low excitation powers, the generated carriers occupy the localized states with lower energies. As the amount of carriers is increased with increased P_{ex} , higher energy states are occupied and therefore the peak of the emitted light shifts to a shorter wavelength. The extended tail in the low energy side of the PL spectra shown in Fig. 6(a) and Fig. 7(a) is an indication of the radiation from these localized states. We have performed a simulation for such effect by assuming a joint density of states associated with the localized states as $\text{erfc}((\langle E_0 \rangle - E)/\Delta E)$, where erfc is the complementary error function, $\langle E_0 \rangle$ and ΔE refer to the average and the standard deviation of the transition energy to take into account of the inhomogeneous broadening effect [32]. ΔE values of 30meV and 18meV were used in the calculation for samples A1 and C1. When the Fermi level is raised because of a higher pumping power, the emission peak blue shifts to a higher energy. The calculated results are shown together with the experiment data in Fig. 7(b). Excellent agreement between the calculated and the experimental results was achieved. Since sample A1 has a broader PL spectrum, it has a larger ΔE and a more pronounced states filling effect. Therefore it has a larger energy shift compared to that of sample C1. In general, both the states filling effect and the band bending effect should contribute to the energy shift. The reason that states filling effect dominates here is due to the large ΔE and the relative small band bending effect in “W” type QWs.

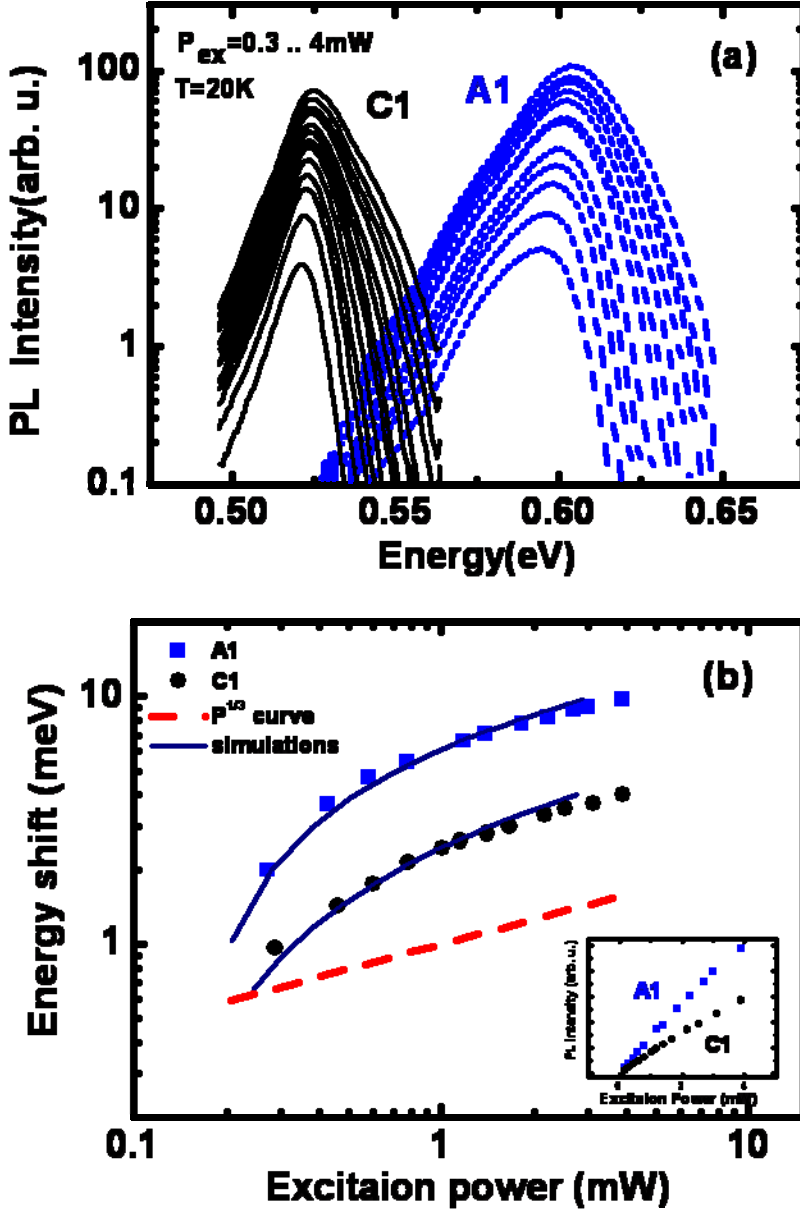


Fig. 7 (a) Power dependence PL spectra of sample A1 and sample C1, and (b) the energy shifts versus P_{ex} along with the simulation results and the ideal $P_{ex}^{1/3}$ curve for comparison. The inset shows the power dependence of the integrated PL intensity.

In order to examine the sample emission at higher temperatures, we have done the PL measurement with the temperature varied from 35K to 290K under a fixed 10mW excitation power. **Figure 8(a)** shows λ_{peak} as a function of temperature for samples A1, B1, B2, and B3. As the temperature raises, the emission wavelength red shifts as expected due to the band gap shrinkage. The cut-off λ_{peak} around $2.56\mu\text{m}$ in the spectrum of sample B3 is caused by the lens absorption in our measure system. The temperature dependence of the emission peak is fitted well with the Varshni relation, $E(T)=E(0)-\alpha T^2/(\beta+T)$, as shown the curves in **Figure 8(a)**. The peak wavelength can be extrapolated to $2.67\mu\text{m}$ at room temperature in sample B3. The temperature dependence of the normalized integrated PL intensity is presented in **Fig. 8(b)**. It shows only about one order

of magnitude reduction in the PL intensity from LT to RT. The reason that the “W” type QWs emission intensity can be well sustained to high temperatures is due to the good carrier confinement and a low density of nonradiative defects in our samples.

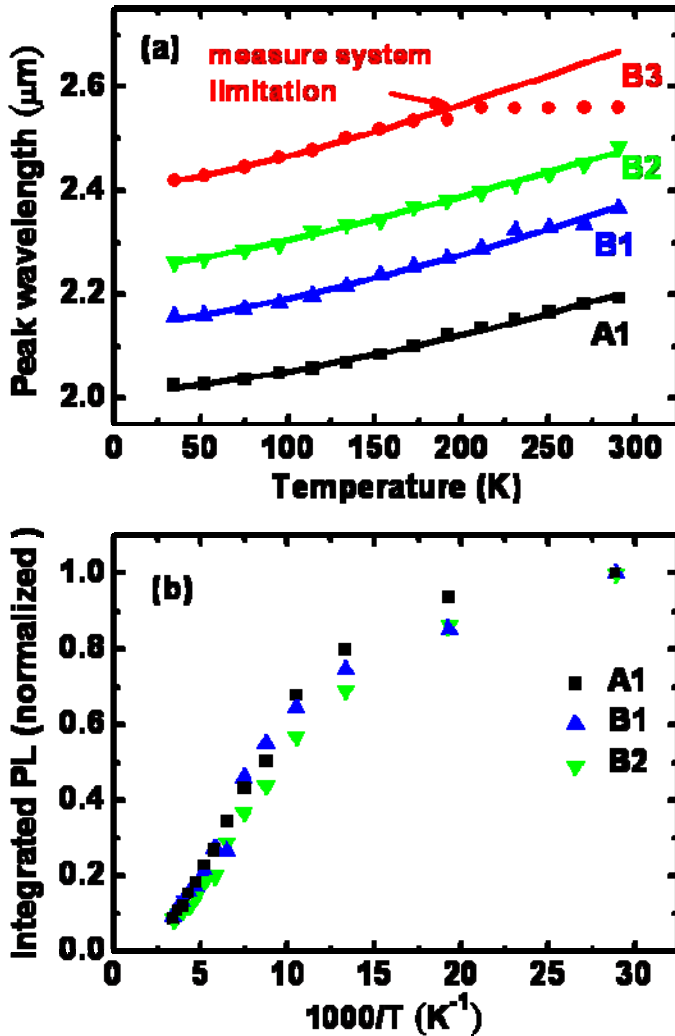


Fig. 8 (a) PL peak wavelength v.s. temperature in sample A1, B1, B2, and B3. (b) Temperature dependence of the normalized integrated PL intensity (points) with the fitted Varshni curves.

3-2 Magneto-optical properties of type-II GaAs QDs in GaSb matrix

A. Structural properties

The TEM samples were taken from sample A. The cross-sectional and plan-view images are presented in Fig. 9(a-b) and 1(c), respectively. The dark areas arising from strain contrast revealed small-sized QDs. From the images, the QDs were estimated to have an aspect ratio of 2.5:1 (width of 9 nm and height of 3.6 nm) and the areal density of $3 \times 10^{11} \text{ cm}^{-2}$. The size distribution was shown in the inset of Fig. 9(c). The average base width of the dots was 6.7 nm, which is smaller than that of the conventional compressively-strained QDs [33, 34]. Because of the small dot size, the confined electron states were expected to be close to that of the wetting layer (WL).

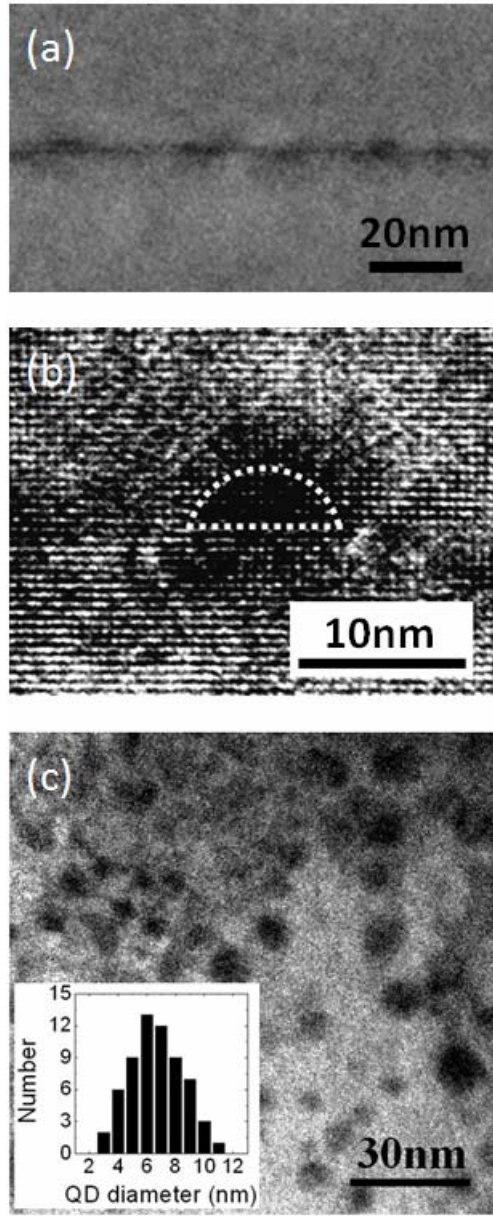


Fig. 9 Cross-section (a) TEM and (b) HRTEM images of GaAs QDs in GaSb matrix along the $[010]_{\text{GaSb}}$ zone axis. We estimated the average width of QDs as 6.7 nm from (c) the plan-view image taken along $[001]_{\text{GaSb}}$ axis. The inset shows the distribution of the QD diameter.

B. Conventional PL and the excitation power dependence

Figure 10 shows the PL spectra of our samples along with that of the GaSb substrate taken as a reference. A broad emission centered at 0.73 eV is seen for all samples (even for the reference sample, the red dotted line). Since this emission energy is below the GaSb band gap of 0.812 eV, it is hence attributed to the impurities or defects within the GaSb substrate. The low energy emissions labeled as A1, B1, and C1 are from the central area of these samples and are attributed to the GaAs QDs. The lowest PL peak energy of 0.564 eV ($\sim 2.2 \mu\text{m}$) is from the largest QDs of sample C1 as a result of the largest amount of deposited GaAs. The PL intensity of C1 is almost half that of A1 due to the more separated electrons and holes for larger type-II dots. Note that the full width at half maximum (FWHM) is 33 meV here, which is smaller than that in Ref. [11] of around 50 meV. The small FWHM indicates that a more uniform QD size distribution, especially in height, is achieved probably by the MEE method.

The dashed lines (labeled as A2 and C2) show the PL from the samples' edge, where the growth temperature is about 20 °C lower than that of the central area. The QDs formed in the edge are therefore expected to be smaller. These emission peaks have the asymmetric shape with a low energy band tail, which may be attributed to the QDs with less uniform size distribution due to lower growth temperature. However, in the next section, the magneto-PL measurement which probes the in-plane spatial extent of the carrier wave function reveals that the origins of these two peaks are from the GaAs WLs. The energy tail has also been found in other Sb-contained or N-contained quantum wells (QWs) and WLs [35-39], and is attributed to the localized states from alloy composition fluctuation, well thickness irregularity, and other crystal imperfections [35].

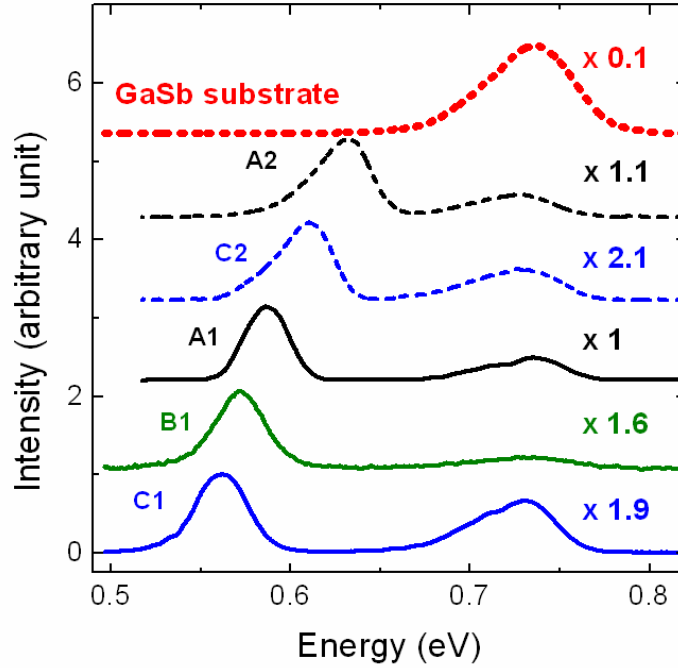


Fig. 2: PL spectra of the three samples and the GaSb substrate. The solid lines, A1, B1, and C1, are from the central area of these samples. The dashed lines, A2 and C2, are from the samples' edge.

As the excitation power increases, all the emission peaks exhibit energy blue shifts, except that from the GaSb substrate. A representative series of power-dependent PL spectra from sample A1 are illustrated in Fig. 11. The blue shift is proportional to the 1/3 power of excitation power as seen in the inset, which is a clear signature of type-II heterostructure. The spatial separation between electrons and holes in the GaAs/GaSb heterostructures leads to the long carrier recombination time and hence the dramatically increased carrier density with the excitation power. The accumulated electrons confined inside the QDs or WLs fill the electron high energy states and induce a triangular potential well in the GaSb next to GaAs and hence raise the energies of holes. These so-called state filling and band bending effects give rise to the energy blue shifts [40, 41].

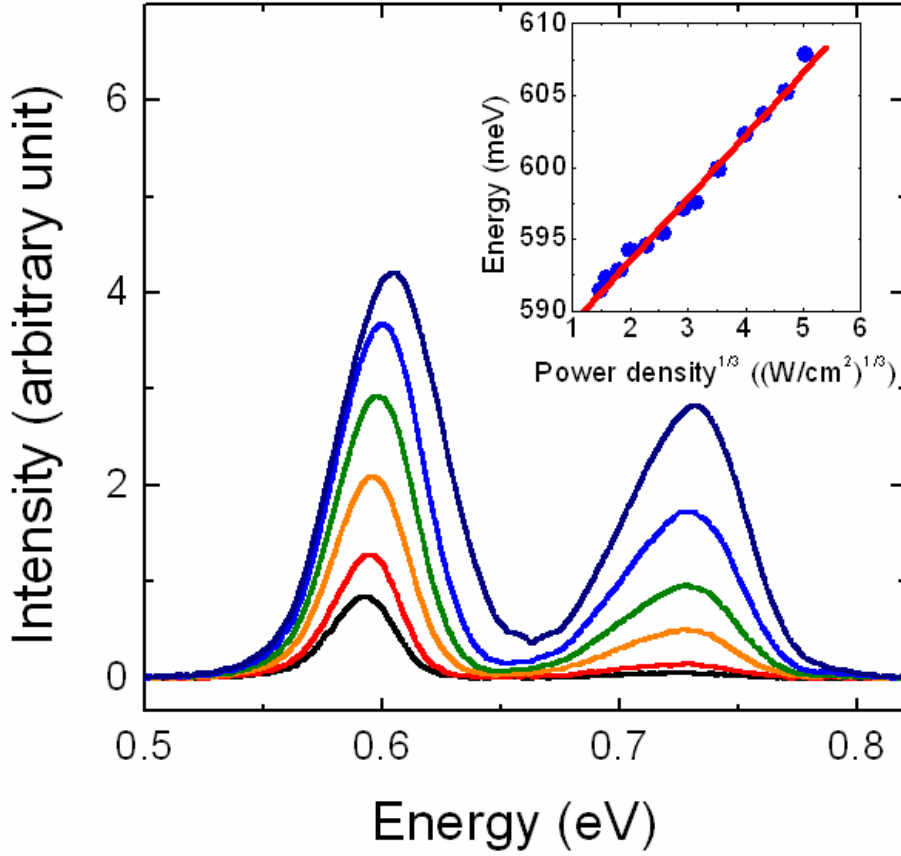


Fig. 11 Representative power-dependent PL spectra from A1. The excitation power density is varied from $4\text{W}/\text{cm}^2$ to $80\text{W}/\text{cm}^2$. The inset shows the emission peak energy of GaAs QDs plotted against the cubic root of the excitation power density.

C. Magneto-PL

The PL spectra of GaAs QDs have been measured as a function of the magnetic field in a Faraday configuration; those from A1 and C1 are shown in Fig. 12. The PL intensity is enhanced with magnetic field (by about 40% at 14 Tesla) due to the additional confinement of carriers from the magnetic field. The blue shift of energy peak, the diamagnetic shift, has a quadratic dependence on magnetic field. The diamagnetic shift can be well described by the following simple equation when the field is relatively low:

$$\Delta E = \beta B^2 = \frac{e^2 \langle \rho_e \rangle^2 B^2}{8m_e} + \frac{e^2 \langle \rho_h \rangle^2 B^2}{8m_h}$$

where β is the diamagnetic coefficient, ρ_e (ρ_h) is the radius of the electron (hole) wave function projected on the plane perpendicular to the magnetic field, m_e (m_h) is the electron (hole) effective mass. The diamagnetic coefficient of the larger QDs from C1 is $7.6 \mu\text{eV}/\text{T}^2$. Interestingly, the smaller QDs from A1 show a considerably larger diamagnetic coefficient of $17.3 \mu\text{eV}/\text{T}^2$, which is more than double that of the larger QDs. This result suggests that the carrier wave function of the smaller QDs is more extended than that of the larger QDs. This behavior is unexpected for regular sized QDs because the wave functions are generally restricted to a smaller area when the dots get smaller [42]. It should be mentioned that the excitation power is kept very low at $1 \text{W}/\text{cm}^2$ for the magneto-PL study to reduce the state filling and band bending effects.

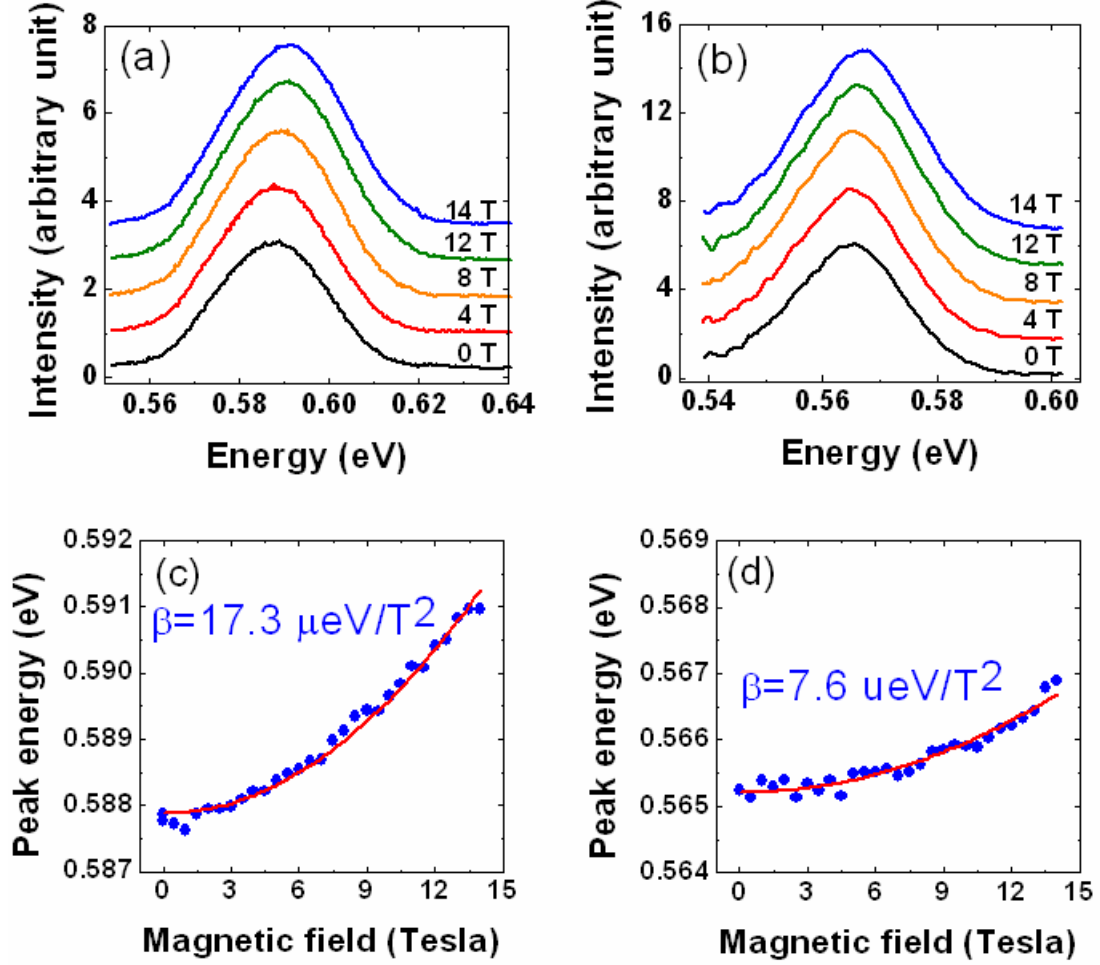


Fig. 12 The magneto-PL spectra from (a) A1 and (b) C1. The emission peak energy is fitted to the square of the magnetic field for (c) A1 and (d) C1.

We have performed the measurements on various locations of the three samples to study the dependence of the diamagnetic coefficient as a function of the emission energy. The result is plotted in Fig. 13. The solid symbols represent the emission peaks with symmetric shapes which are assigned as QD optical transitions. On the other hand, the open symbols represent the asymmetric emissions with low energy band tails. The diamagnetic coefficient first increases quickly with the emission energy for the QD emissions and then saturates around $21 \mu\text{eV}/\text{T}^2$ for those asymmetric emissions. This saturated stable diamagnetic coefficient indicates that the in-plane spatial extent of the carrier wave function is almost independent of the confinement potential. We therefore convincingly attribute those asymmetric emissions as type-II WL emissions. The diamagnetic shift of WL in a Faraday configuration depends on the electron-hole separation. For type-I QWs with infinite barriers, the electron-hole separation decreases as the well thickness is reduced due to the enhancement of their Coulomb interaction [43]. However, the spatially separated electron-hole pair of type-II structure causes the lateral separation less sensitive to the well thickness.

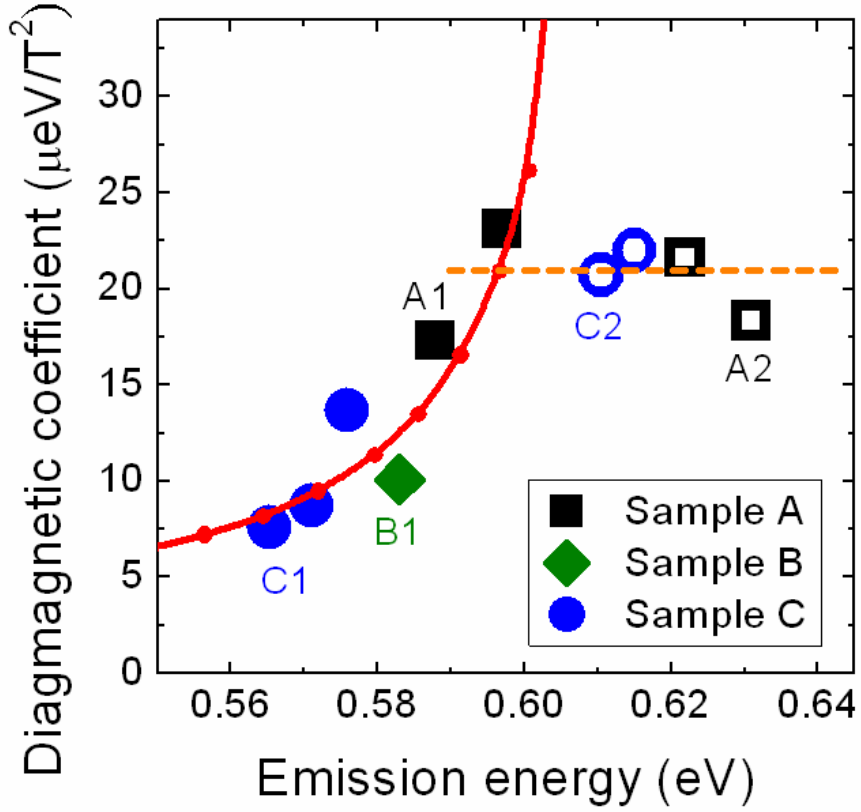


Fig. 13 The diamagnetic coefficient against the emission energy of sample A (black squares), sample B (green diamonds), and sample C (blue circles). The solid (open) symbols represent the emissions with symmetric (asymmetric) PL shapes. The calculation results are also plotted here as the red solid line.

Now we turn to the QD emissions. We attribute the increase of the diamagnetic shift with emission energy to two specific properties of the GaAs/GaSb QDs: the tensile-strained system and the small QD dimension. Unlike the common compressively-strained system, where the partial strain-relaxation and the larger height (compared to WL) make the QD energy much lower than that of the WLs, the tensile-strain-relaxation within the GaAs/GaSb QDs substantially raises the band gap energy and compensates the effect of the larger height of the QD. The electron ground state of the QDs hence gets close to or even goes beyond that of the WL, which is fully strained, as the QDs get smaller. As a consequence, the electrons spread out of the QD to the WL, therefore causing an increased diamagnetic coefficient, which eventually saturates at that of the WL.

D. Simulation

We have calculated the electron wave functions using one-band effective mass Hamiltonian. The diameter of the lens-shaped QDs with an aspect ratio of 2.5:1 is varied from 4 nm to 28 nm. A WL of 1 nm thickness is placed below the QD. The composition of the QD, the WL, and the matrix is taken as $\text{GaAs}_{0.8}\text{Sb}_{0.2}$, $\text{GaAs}_{0.45}\text{Sb}_{0.55}$, and $\text{GaAs}_{0.1}\text{Sb}_{0.9}$ to account for partial intermixing of As and Sb atoms during growth [11, 44]. Besides, the WL and the pseudomorphically grown matrix are taken to be fully-strained matching the lattice constant of GaSb [11], but the QD is assumed to be 25% strain relaxed. The band diagram of a QD and the adjacent WL under full strain (dotted line) and with the partially relaxed strain in the QD for

light-hole state (solid line) and the heavy-hole state (dashed line) is illustrated in the inset of Fig. 14(a). The parameters used in the calculation are taken from Ref. [45]. Due to the small dot size and large conduction band offset (480 meV), the electrons are confined inside the dot at a high quantization energy. The effective mass is therefore taken as high as $0.08 m_0$ owing to the conduction band nonparabolicity [46]. The diamagnetic response can be further calculated by superimposing a magnetic confining potential to the Hamiltonian and then fitted to $\Delta E = \beta B^2$ to find the electron-contributed diamagnetic coefficient.

Holes are confined to the Ga(As)Sb region near the QD in this type-II system due to the Coulomb attraction to electrons. However, the complicated strain distribution near the QD (with compressive strain in the vicinity of the dot and tensile strain elsewhere) is expected to distort the potential profile for holes and mix the light hole and heavy hole states. To simplify the calculation, we assume that the hole wave function has the same radius as that of the electron wave function, and the hole effective mass is taken to be $0.23 m_0$, which is the average of the heavy hole and light hole effective mass of GaSb. Consequently, the hole-contributed diamagnetic coefficient is about 1/3 of the electron-contributed one.

The calculated transition energy and the corresponding diamagnetic coefficient are plotted in Fig. 14(a) against the diameter of the QD. When the diameter of the QD is larger than 11.5 nm, the diamagnetic coefficient increases with the QD diameter as expected for regular sized QDs. However, as the QD diameter gets smaller than 11.5 nm, the wave function starts to spread into the WL, the transition energy is approaching to the WL emission energy, and the corresponding diamagnetic response is significantly enhanced. Since the GaAs QDs in GaSb matrix are usually very small and all the dots used in this work are smaller than 11 nm, the rising trend of the diamagnetic coefficient is observed as the QDs get smaller. To compare with the experimental data, the calculated diamagnetic coefficient is plotted (for the small dots) as a function of the transition energy as the red solid lines in Fig. 13 and 14(b). It agrees very well with the experimental data until the rising diamagnetic coefficient exceeds that of the WL at $21 \mu\text{eV}/\text{T}^2$, the orange dashed line. In this situation, the electron-hole Coulomb interaction starts to play an important role, and this simplified model becomes invalid. In Fig. 14(b), by defining the QD and WL region as the inset, we calculate the fraction of the electron localized in the QD and plot it as the green line. In the calculation, the electron wave function dramatically spreads out of the QD to the WL as the diamagnetic coefficient gets larger than $21 \mu\text{eV}/\text{T}^2$, the experimental value of the WL.

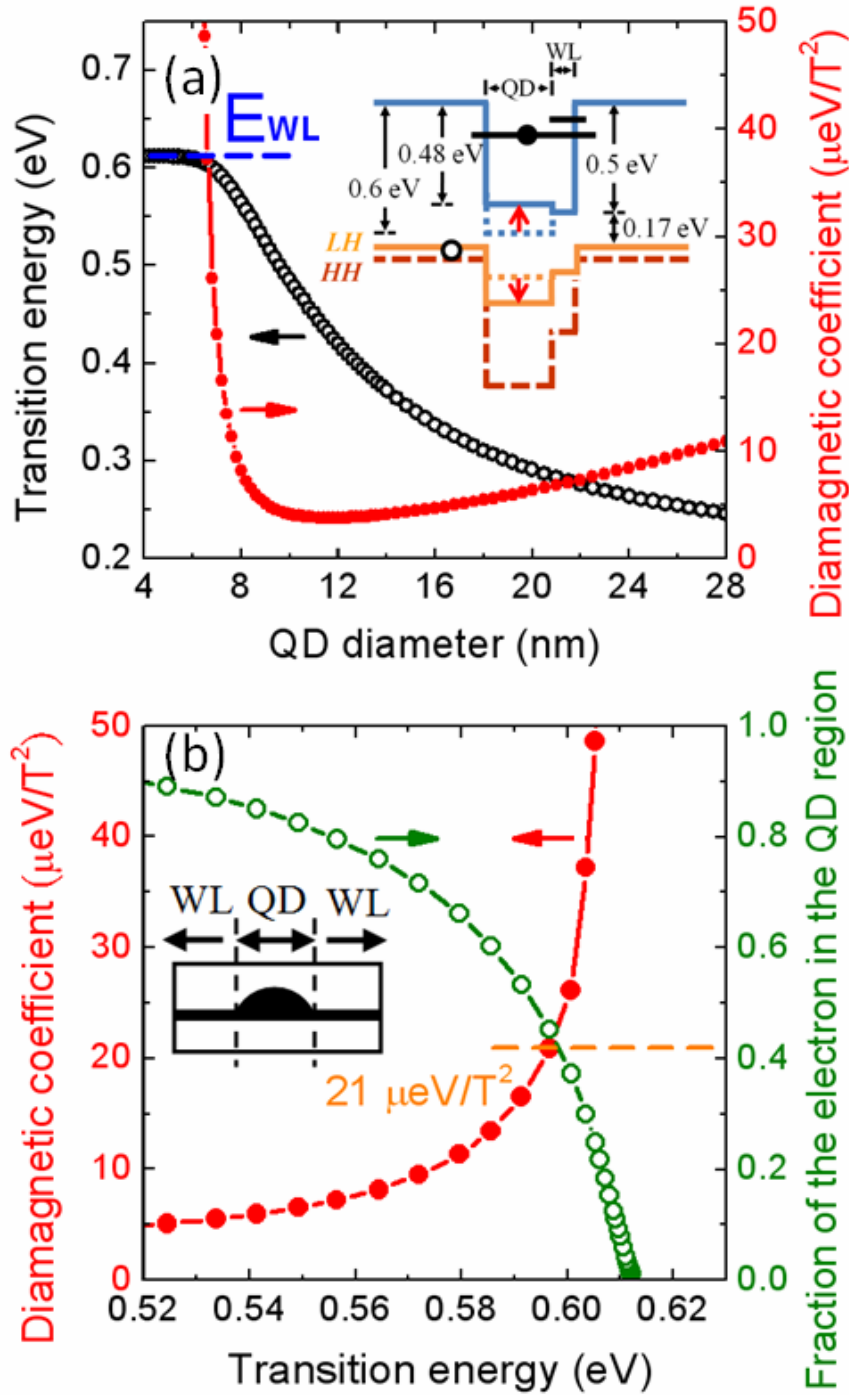


Fig. 14 (a) The calculated transition energy and the corresponding diamagnetic coefficient with the diameter of the QD. The inset shows the band diagram of a QD and the adjacent WL under full strain (dotted line) and with the 20% relaxed strain in the QD for the light-hole state (solid line) and for heavy-hole one (dashed line). (b) The diamagnetic coefficient and the fraction of the electron localized in the QD region against the transition energy. The regions of QD and WL are defined as illustrated in the inset.

3-3 Sb-based high speed electronic devices

The actual epitaxial structure (Rn0750) was shown in Fig. 15. First, 10 pairs of AlSb quantum dots (QDs) capped with a thin layer of GaAs (10 nm) were grown as the nucleation layer on the (100) semi-insulating GaAs substrate using Veeco MBE. Then a 1.6 μm AlSb thick buffer layer and 300 nm $\text{Al}_{0.7}\text{Ga}_{0.3}\text{Sb}$ were

grown on it. The active layers begins with 15nm bottom AlSb barrier, followed by the 15nm composite channel layers (In_{0.65}As_{0.35}Sb, InAs), 15nm top AlSb barrier with Te as the modulation doping and the In_{0.5}Al_{0.5}As cap layer. The sheet resistance of Al_{0.7}Ga_{0.3}Sb buffer measured by the four-point probe was around 4300 ohm/□. The surface of the epitaxial structure measured by AFM showed smooth surface morphology, with its roughness around 5-7 nm, as shown in Fig. 16. The room-temperature Hall measurement showed the channel electron concentration and mobility are 1.18x10¹² cm⁻² and 10134 cm²/Vs, respectively. The channel sheet resistance is 521 ohm/□.

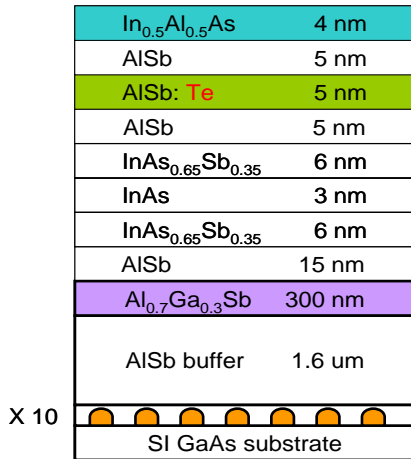


Fig. 15 The schematic diagram of the epitaxial structure of sample Rn0750

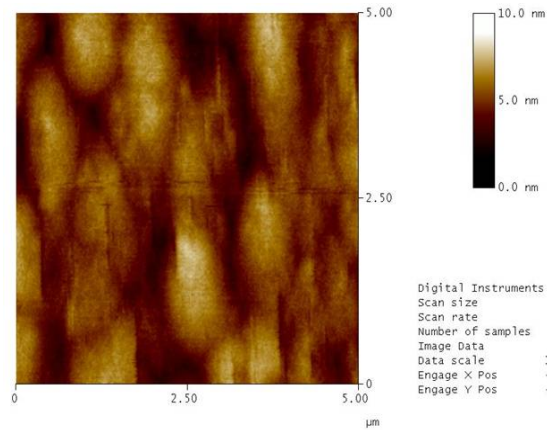


Fig. 16 The surface roughness image of sample Rn0750 measured by AFM

The device fabrication begins with Pd/Pt/Au ohmic contact deposition, which was annealed at 300°C for 30s. Then the isolation mesa was defined by the HF-based wet chemical etch solution. After isolation mesa formed, LT-SiN was performed to protect the exposed Al_{0.7}Ga_{0.3}Sb buffer from oxidation. Finally, the Ti/Au Schottky gate was deposited by the e-beam evaporation. The device dc characteristics measured by HP4145 was shown in Fig. 17. The gate length and device width of the device are 2μm and 50 μm, respectively. The device exhibited modulation with V_{gs} from 0.1V to -0.4V. The maximum drain current is around 110 mA/mm at V_{gs}=0.1V and V_{ds}=0.5V. The device can not be pinched off completely yet and performed leakage current, which is around 2.5 mA at V_{gs}= -0.4V and V_{ds}= 0.5V. The transconductance of the device was ~ 60 mS/mm. The Schottky gate I-V was showed in Fig. 18. The forward turn-on voltage was 0.75V and the reverse characteristics showed a low leakage current ~250uA at V_{gs}= -1V and a high reverse breakdown voltage of above 1V.

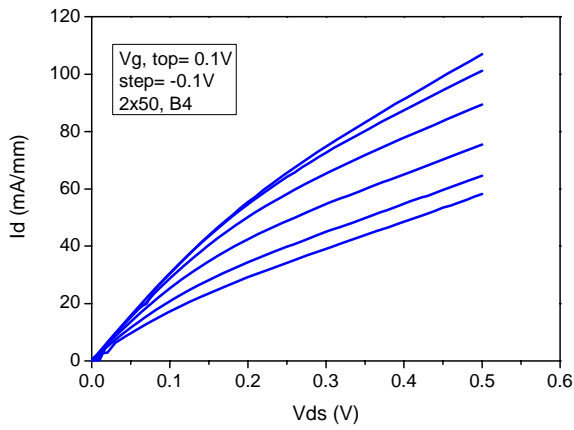


Fig. 17 The device IV characteristics of sample Rn0750

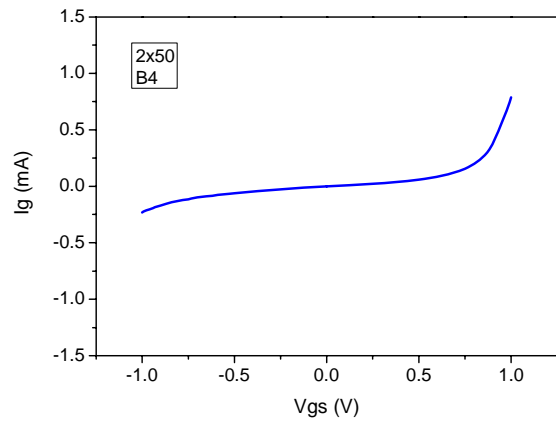


Fig. 18 The device Schottky IV characteristics of sample Rn0750

In order to further improve device pinch-off problem, we designed another buffer layer structure (Rn0791), hoping to further increase the resistance of buffer layer. The actual epitaxial structure was shown in Fig. 19. First, 10 pairs of AlSb quantum dots (QDs) capped with GaAs (10 nm) were grown on the (100) semi-insulating GaAs substrate as the nucleation layer. Then a 1.1 μm AlSb thick buffer layer and 300 nm $\text{Al}_{0.8}\text{Ga}_{0.2}\text{Sb}$ were grown on it. In addition, a InSb QDs layer was inserted at the location 300 nm from the bottom nucleation layer to further accommodate the dislocation due to the lattice mismatch between the AlSb buffer layer and the GaAs substrate. The active layer was the same as that of sample Rn 0750. The sheet resistance of $\text{Al}_{0.8}\text{Ga}_{0.2}\text{Sb}$ buffer was around 25000 ohm/\square , which was much higher than that of sample Rn0750 (4300 ohm/\square). The surface of the epitaxial structure showed the same smooth surface morphology as that of sample Rn0750, with its roughness around 6-8 nm, as shown in Fig. 20. The room-temperature Hall measurement showed the channel electron concentration and mobility are $7.91 \times 10^{11} \text{ cm}^{-2}$ and $12000 \text{ cm}^2/\text{Vs}$, respectively. The channel sheet resistance is 727 ohm/\square .

The device dc characteristics was shown in Fig. 21. The gate length and device width of the device are 2 μm and 50 μm , respectively. As can be seen, the device exhibited modulation with V_{gs} from 0.1V to -0.4V. The maximum drain current is around 40 mA/mm at $V_{\text{gs}}=0.1\text{V}$ and $V_{\text{ds}}=0.5\text{V}$. The device performed a much lower leakage current ($\sim 1.5 \text{ mA}$) than that of sample Rn0750 at $V_{\text{gs}}= -0.4\text{V}$ and $V_{\text{ds}}= 0.5\text{V}$, although it can not be pinched off completely yet.

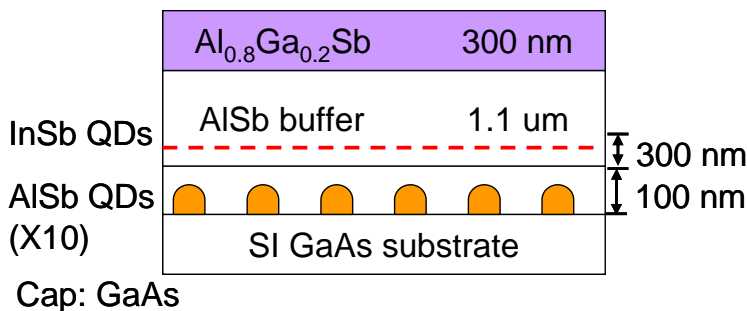


Fig. 19 The schematic diagram of the buffer layer structure of sample Rn0791

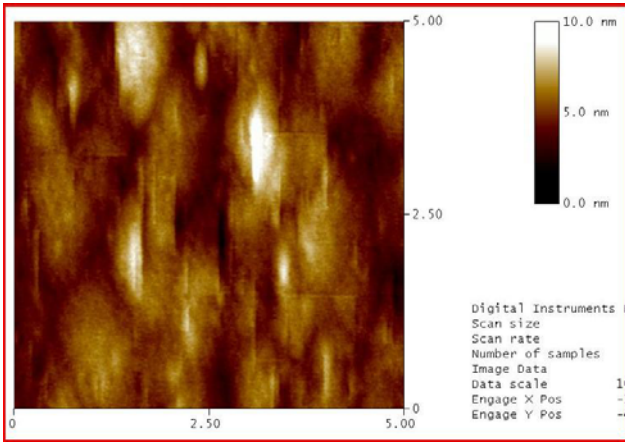


Fig. 20 The surface roughness image of sample Rn0791 measured by AFM

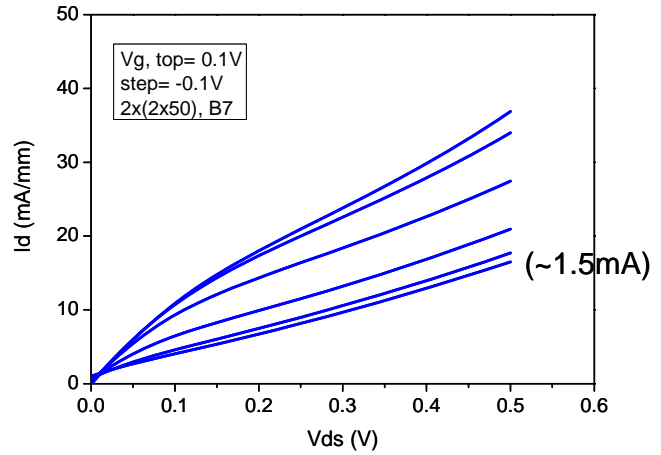


Fig. 21 The device IV characteristics of sample Rn0791

4. Conclusion

In this project, first, we have studied the InGaAs/GaAsSb/InAlGaAs/InAlAs “W” type QWs grown on InP substrates. The emission wavelength covers the range from ~ 2 to ~ 2.5 μm at low temperature. The trade-off between long wavelength emission and high optical matrix element predicted by the simulation has been confirmed by the results of PL spectra. The type-II band alignment in the “W” structure has been characterized by the power dependent PL measurements. The peak position shifts to shorter wavelength as P_{ex} increases. It was found the amount of energy shifts does not follow the $P_{\text{ex}}^{1/3}$ law as most type II structures. The localized states filling effect due to the surface roughness and alloy fluctuation is proposed to explain the observed phenomenon. The calculated results agree well with the experiment results. The temperature dependent PL spectra show the well sustained emission at RT, and the emission wavelength of the “W” type QWs can be extended to over 2.56 μm . According to our experiments and simulation results, it is very promising to develop the Mid-IR lasers on InP substrates employing the “W” structure of InGaAs/GaAsSb/InGaAs QWs.

Next, type-II tensily-strained GaAs QDs in GaSb with mid-IR emission up to 2.2 μm were studied by magneto-PL for the first time. By comparing several samples with different GaAs deposition amount, the diamagnetic coefficient was found to rise quickly from 7.6 $\mu\text{eV}/\text{T}^2$ to a saturated value of around 21 $\mu\text{eV}/\text{T}^2$ with the emission energy. This unusual behavior is due to the spreading of the electron wave function from the QD to the WL as the dots get smaller. A theoretical calculation of the diamagnetic shift in this type-II QD system considering the strain effect is performed and the results agree with the experimental finding.

Finally, we successfully grew samples with electron mobility ~ 12000 cm^2/Vs for the application of Sb-based high speed electronic device. The sheet resistance of buffer layer was further improved from 4300 ohm to 25000 ohm by using a two-layer QD buffer structure. The corresponding device performance showed good modulation characteristics and lower buffer leakage current (1.5 mA) at pinch-off condition. The Schottky gate also performed good forward turn-on and reverse low leakage current characteristics. We will continue to improve device isolation to realize a Sb-based HFET with complete pinch-off, high mobility and high breakdown voltage.

Reference

- [1] U. Willer, M. Saraji, A. Khorsandi, P. Geiser, and W. Schade, *Opt. Lasers Eng.* **44**, 699 (2006).
- [2] A. Godard, *C. R. Phys.* **8**, 1100 (2007)
- [3] W. Li, J. B. Héroux, H. Shao, and W. I. Wang, *Appl. Phys. Lett.* **84**, 2016 (2004).
- [4] J. A. Gupta, P. J. Barrios, J. Lapointe, G. C. Aers and C. Storey, *Appl. Phys. Lett.* **95**, (2009).
- [5] G. K. Kuang, G. Bohm, M. Grau, G. Rosel, R. Meyer, and M.-C. Amann, *Appl. Phys. Lett.* **77**, 1091 (2000).
- [6] T. Sato, M. Mitsuhashi, N. Nunoya, T. Fujisawa, F. Kano, Y. Kondo, *IEEE Photonics Technol. Lett.* **20**, 1045 (2008).
- [7] M. Geller, C. Kapteyn, L. Müller-Kirsch, R. Heitz, and D. Bimberg, *Appl. Phys. Lett.* **82**, 2706 (2003).
- [8] H. Gotoh, H. Ando, H. Kamada, A. Chavez-Pirson, and J. Temmyo, *Appl. Phys. Lett.* **72**, 1341 (1998).
- [9] E. Ribeiro, A. O. Govorov, W. Carvalho, Jr, and G. Medeiros- Ribeiro, *Phys. Rev. Lett.* **92**, 126402 (2004).
- [10] I. R. Sellers, V. R. Whiteside, I. L. Kuskovsky, A. O. Govorov, and B. D. McCombe, *Phys. Rev. Lett.* **100**, 136405 (2008).
- [11] A. A. Toropov, O. G. Lyublinskaya, B. Ya. Meltser, V. A. Solov'ev, A. A. Sitnikova, M. O. Nestoklon, O. V. Rykhova, S. V. Ivanov, K. Thonke and R. Sauer, *Phys. Rev. B* **70**, 205314 (2004)
- [12] B. R. Bennett, R. Magno, J. B. Boos, W. Kruppa and M/ G. Ancona, *Solid-State Electron* **49**, 1875 (2005)
- [13] B. Brar and H. Kroemer, *IEEE Electron Device Lett.* **16**, 548 (1995)
- [14] C. R. Bolognesi, M. W. Dvorak, and D. H. Chow, *IEEE Trans. Electron. Device* **46**, 826 (1999)
- [15] C. R. Bolognesi, and D. H. Chow, *IEEE Electron. Device Lett.* **17**, 534 (1996)
- [16] J. B. Boos, M. J. Yang, B. R. Bennett, D. Partk, W. Kruppa, C. H. Yang and R. Bass, *Electron. Lett.* **34**, 1525 (1998)
- [17] H.-K. Lin, C. Kadow, M. Dahlström, J. -U. Bae, M. J. W. Rodwell, A. C. Gossard, B. Brar, G. Sullivan, G. Nagy, and J. Bergman, *Appl. Phys. Lett.* **84**, 437 (2004)
- [18] H.-K. Lin, C. Kadow, J. -U. Bae, M. J. W. Rodwell, A. C. Gossard, B. Brar, G. Sullivan, G. Nagy, and J. Bergman, *J. Appl. Phys.* **97**, 024505 (2004)
- [19] J. B. Boos, M. J. Yang, B. R. Bennett, D. Partk, W. Kruppa and R. Bass, *Electron. Lett.* **35**, 847 (1999)
- [20] J. Y. T. Huang, D. P. Xu, L. J. Mawst, T. F. Kuech, I. Vurgaftman, and J. R. Meyer, *IEEE J. Sel. Top. Quantum Electron.* **13**, 1605 (2007).
- [21] J. Hu, X. G. Xu, J. A. H. Stotz, S. P. Watkins, A. E. Curzon, M. L. W. Thewalt, N. Matine and C. R. Bolognesi, *Appl. Phys. Lett.* **73**, 2799 (1998).
- [22] C. Pryor and M.-E. Pistol, *Phys. Rev. B* **72**, 205311 (2005).
- [23] I. Vurgaftman, J. R. Meyer, and L. R. Ram-Mohan, *J. Appl. Phys.* **89**, 5815 (2001).
- [24] M. J. Yang, B. R. Bennett, M. Fatemi, P. J. Lin-Chung, W. J. Moore and C. Y. Yang, *J. Appl. Phys.* **87**, 8192 (2000)
- [25] C. E. Pryor and M. E. Pistol, *Phys. Rev. B* **72**, 205311 (2005)
- [26] C. Renard, X. Marcadet, J. Massies and O. Parillaud, *J. Crystal Growth* **278**, 193 (2005).
- [27] J. F. Klem, O. Blum, S. R. Kurtz, I. J. Fritz, and K. D. Choquette, *J. Vac. Sci. Technol. B* **18**, 1605 (2000).
- [28] M. C. Lo, S. J. Huang, C. P. Lee, S. D. Lin and S. T. Yen, *Appl. Phys. Lett.* **90** (2007).

- [29] N. N. Ledentsov, J. Böhrer, M. Beer, F. Heinrichsdorff, M. Grundmann, D. Bimberg, S. V. Ivanov, B. Ya. Meltser, S. V. Shaposhnikov, I. N. Yassievich, N. N. Faleev, P. S. Kop'ev and Zh. I. Alferov, *Phys. Rev. B* **52**, 14058 (1995).
- [30] M. Dinu, J. E. Cunningham, F. Quochi, and J. Shah, *J. Appl. Phys.* **94**, 1506 (2003).
- [31] A. Ait-Ouali, R. Yip, J. Brebner and R. Masut, *J Appl Phys* **83**, 3153 (1998).
- [32] J. Christen and D. Bimberg, *Phys. Rev. B* **42**, 7213 (1990).
- [33] H. Saito, K. Nishi, and S. Sugou, *Appl. Phys. Lett.* **74**, 1224 (1999).
- [34] F. Hatami, N. N. Ledentsov, M. Grundmann, J. Böhrer, F. Heinrichsdorff, M. Beer, D. Bimberg, S. S. Ruvimov, P. Werner, U. Gösele, J. Heydenreich, U. Richter, S. V. Ivanov, B. Ya. Meltser, P. S. Kop'ev, and Zh. I. Alferov, *Appl. Phys. Lett.* **67**, 656 (1995).
- [35] M. Dinu, J. E. Cunningham, F. Quochi, and J. Shah, *J. Appl. Phys.* **94**, 1506 (2003)
- [36] M. C. Lo, S. J. Huang, C. P. Lee, S. D. Lin, and S. T. Yen, *Appl. Phys. Lett.* **90**, 243102 (2007).
- [37] Y.-H. Cho, T. J. Schmidt, S. Bidnyk, G. H. Gainer, J. J. Song, S. Keller, U. K. Mishra, and S. P. DenBaars, *Phys. Rev. B* **61**, 7571 (2000).
- [38] J. Bai, T. Wang, and S. Sakai, *J. Appl. Phys.* **88**, 4729 (2000).
- [39] F. Ishikawa, Á. Guzmán, O. Brandt, A. Trampert, and K. H. Ploog, *J. Appl. Phys.* **104**, 113502 (2008).
- [40] W. H. Chang, Y. A. Liao, W. T. Hsu, M. C. Lee, P. C. Chiu, and J. I. Chyi, *Appl. Phys. Lett.* **93**, 033107 (2008).
- [41] N. N. Ledentsov, J. Böhrer, M. Beer, F. Heinrichsdorff, M. Grundmann, D. Bimberg, S. V. Ivanov, B. Ya. Meltser, S. V. Shaposhnikov, I. N. Yassievich, N. N. Faleev, P. S. Kop'ev, and Zh. I. Alferov, *Phys. Rev. B* **52**, 14058 (1995).
- [42] M. Sugisaki, H. W. Ren, S. V. Nair, K. Nishi, and Y. Masumoto, *Phys. Rev. B* **66**, 235309 (2002).
- [43] S. N. Walck and T. L. Reinecke, *Phys. Rev. B* **57**, 9088 (1998)
- [44] R. Timm, H. Eisele, A. Lenz, S. K. Becker, J. Grabowski, T.-Y. Kim, L. Müller-Kirsch, K. Pötschke, U. W. Pohl, D. Bimberg, and M. Dähne, *Appl. Phys. Lett.* **85**, 5890 (2004).
- [45] I. Vurgaftman, J. R. Meyer, and L. R. Ram-Mohan, *J. Appl. Phys.* **89**, 5815 (2001).
- [46] D. F. Nelson, R. C. Miller, and A. A. Kleinman, *Phys. Rev. B* **35**, 7770 (1987)